The Dissertation Committee for Hao Li Certifies that this is the approved version of the following Dissertation:

Catalytic Reactions at Alloy Surfaces

Committee:

Graeme Henkelman, Supervisor

Charles Buddie Mullins

Gyeong Hwang

Simon Humphrey

Catalytic Reactions at Alloy Surfaces

by

Hao Li

Dissertation

Presented to the Faculty of the Graduate School of

The University of Texas at Austin

in Partial Fulfillment

of the Requirements

for the Degree of

DOCTOR OF PHILOSOPHY

The University of Texas at Austin

December 2019

Dedication

I dedicate this work to my grandfather.

Acknowledgements

I'm grateful to Prof. Graeme Henkelman for all of his generous supports, teaching, and guidance to me during these years. He is my "academic father" who teaches me everything in science.

I'm also grateful to all of my excellent scientific collaborators inside and outside of The University of Texas at Austin, including Mr. Hongyu Guo, Dr. Edward J. Evans, Dr. Kihyun Shin, Mr. Ryan Ciufo, Dr. Wenrui Chai, Dr. Aliya Lapp, Mr. Chenxu Yan, Dr. Yulu Liu, Mrs. Huiling Zheng, Dr. Graham Piburn, Mr. Zhiwei Fang, Dr. Penghao Xiao, Prof. Simon Humphrey, Prof. C. Buddie Mullins, Prof. Richard M. Crooks, Prof. Charles J. Werth, Prof. Guihua Yu, Prof. Long Luo (Wayne State University), Prof. Judith C. Yang (University of Pittsburg), Dr. Sujin Guo and Prof. Michael S. Wong (Rice University), Mr. Stephen Xie and Prof. Richard G. Hennig (University of Florida), Dr. Anne Marie Tan and Prof. Dallas Trinkle (University of Illinois at Urbana-Champaign), Dr. Li Wei and Prof. Yuan Chen (The University of Sydney), and Dr. Bing Yu and Dr. Tianyi Ma (University of Newcastle, Australia). I enjoy every single moment of our fantastic collaborations. I appreciate our Graduate Program Coordinator, Mrs. Betsy Hamblen, for all of her help to me during the past four years. I'm also grateful for all the financial supports in my research, including the NSF, DOE, and Welch foundations, and the 2017 Hamilton/Schoch Fellowship, 2018 Department Excellence Fellowship, and 2019 University Graduate Continuing Fellowship. I also appreciate the NSF Institute for Pure & Applied Mathematics at the University of California, Los Angeles, for providing the fantastic platform of scientific workshops and collaborations.

I appreciate my wife, Zijun Li, and my baby daughter, Mia Li, for making my life so beautiful. We look forward to the upcoming adventures in Europe. I'm grateful to my farther, Li Zhuohua, and my mother, Wu Shizhen, for bringing me to this beautiful world.

Finally, I dedicate this work to my grandfather, Li Weixue, who passed away in August last year. He was the man who raised me up, taught me how to be a good person, and protected me during my whole childhood.

Abstract

Catalytic Reactions at Alloy Surfaces

Hao Li, Ph.D.

The University of Texas at Austin, 2019

Supervisor: Graeme Henkelman

Alloys have been widely studied for heterogeneous catalysis. Many bi- and multi-metallic alloys have enhanced performance as compared to their monometallic counterparts. However, a full understanding of the alloying effects was not well-established. In my Ph.D. works, density functional theory (DFT) was employed to disentangle the atomic ensemble, ligand, and strain effects of surfaces alloyed by transition metals. It is found that alloying elements with strong and weak adsorption properties could produce a surface ensemble with optimally tuned adsorbate binding, which can help to understand the mechanisms of catalytic reactions and design high-performance alloy catalysts. We developed a *Tunability* theory that quantifies the tuning of adsorbate bindings at the specific atomic ensembles on surface, which provides predictive power of theory for experiments. Using combined theoretical and experimental methods, we designed and studied new alloy catalysts for many industrially significant reactions including electrocatalysis, vapor-phase catalysis, and liquid-phase catalysis. We developed comprehensive theories that predominantly based on the atomic ensemble effect to unify theories and experiments for alloy heterogeneous catalysts. Most importantly, we show how fundamental understandings from theories can be precisely applied to efficient energy

and environmental reactions. In addition, to accelerate atomistic simulations and materials design, we have been developing a machine learning framework that can fit the potential energy surfaces from the quantum mechanical data, which can help to partly replace expensive DFT calculations and reduce scientific costs.

Table of Contents

List of Figures

Chapter 1: Introduction

The rational design of catalysts remains a huge challenge due to the highly complicated reaction networks and the variety of reaction selectivities. During the past decades, a trial-and-error strategy has been widely applied in new catalytic materials design, which dramatically raises the experimental budget and time consumed. Fortunately, theoretical computation and modeling emerged as powerful tools to understand the reaction mechanism and afford rational predictions, which may potentially replace the conventional trial-and-error process. During my Ph.D. works, we gradually developed a research philosophy that helps to unify the theory, modeling, and experiments in catalysis research. Density functional theory (DFT) calculation, molecular dynamic (MD) simulation, and numerical catalytic modeling can be developed to provide predictive guidance for experiments. In return, the experimental validation and refinement with minimized cost can offer improved mechanistic insights to understand the reaction. Eventually, based on the experimental results, a deeper mechanistic insight can be understood from more detailed computations. This theory-experiment-theory research philosophy can effectively realize rapid catalyst design towards a complicated reaction network, which has shown great efficiency in addressing scientific challenges in many of our recent works (Figure 1).[1-19]

On the other hand, DFT calculations are sometimes too expensive for relatively large atomistic systems even with high-performance computing resources. To provide an alternative to partly replace these calculations, we have been focusing on developing new machine learning methods and packages that can learn from the limited amount of quantum mechanical data (e.g., the structure, energy, and forces from DFT calculations), and perform precise predictions on the energy and forces of those out-of-sample structures.

Together with the research cycle mentioned in Figure 1, our research on new functional materials can be dramatically expedited through these highly integrated modeling, theoretical, and experimental methods.

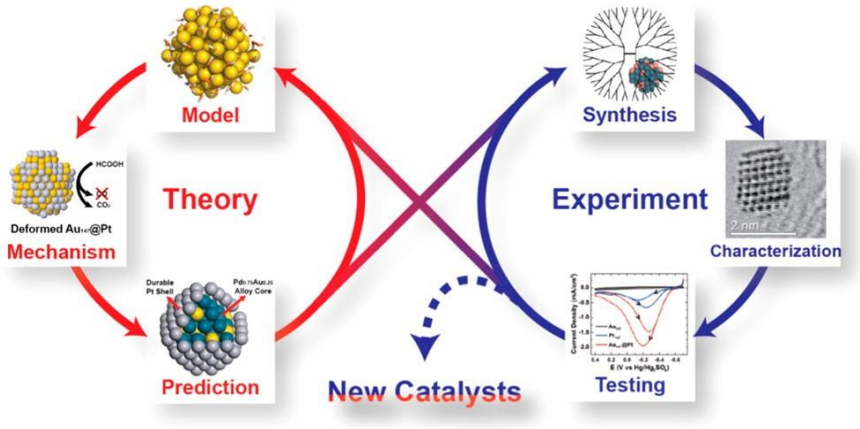

Figure 1.1: A theory-experiment-theory philosophy can dramatically facilitate the rational design of catalysts. Reproduced with permission from Ref.[20].

In general, the topics of my Ph.D. research include both theory and computational methodology development, which can be summarized as: i) disentangling the alloying effects of catalytic surfaces, ii) rational design of effective alloy catalysts by a combined theoretical and experimental strategy, and iii) developing machine learning frameworks to accelerate atomistic simulations.

Chapter 2: Disentangling the Alloying Effects*

2.1 INTRODUCTION

Alloying transition metals with strong and weak adsorption properties can produce a catalyst with optimally tuned adsorbate binding.[11,21] However, a full understanding of this alloying effect was not well-established due to the limits of current experimental characterization techniques. In this study, DFT calculations were performed to disentangle the effects of ensemble,[22] ligand,[23] and strain[24] of close-packed surfaces alloyed by transition metals. Considering PdAu, RhAu, and PtAu bimetallics as the examples, we calculated the tuning of H and O binding energies as a function of lattice constant (strain effect), number of alloy-substituted sublayers (ligand effect), and randomly alloyed geometries (atomic ensemble effect). We found that on the PdAu, RhAu, and PtAu alloyed surfaces, ensemble effects more significantly influence the adsorbate binding as compared to the effects of ligand and strain, indicating that the H and O bindings are predominantly determined by the local atomistic environment provided by the specific triatomic ensemble. We also found similar conclusions on other commonly studied bimetallic alloys. Based on these discoveries, we developed a *Tunability* theory that describes the tuning trends of H bindings at PdAu and PtAu surfaces and provided precise predictive guide for C=C hydrogenation experiments.[15]

2.2 COMPUTATIONAL METHODS

The DFT calculations were performed with the Vienna *Ab initio* Simulation Package (VASP). Kohn–Sham (KS) wave functions were expanded in a plane wave basis to describe the valence electrons with the energy cutoff set as 400 eV.[25] Generalized

* Li, H.; Shin, K.; Henkelman, G. *J. Chem. Phys.* **2018**, 149 (17), 174705; Li, H. proposed the idea, designed the research, conducted the modeling and DFT calculations, and wrote the paper.

gradient approximation (GGA) method with Perdew–Burke–Ernzerhof (PBE) functional was employed to describe electronic exchange and correlation.[26] A projector augmented-wave (PAW) method was employed to describe core electrons.[27] Geometries were considered optimized when all the forces in the atomistic system fell below 0.05 eV/Å. For the calculations of slab models, the Brillouin zone was sampled by a (3 × 3 × 1) Monkhorst–Pack (MP) *k*-point mesh.[28] For the cluster models, gamma point was used for the sampling. Spin polarization was tested and used when necessary. More computational and modeling details can be found in Ref.[4].

2.3 Results and Discussion

On close-packed structures, a triatomic ensemble in a 3-fold symmetry is the smallest repeat unit that describes the adsorption environment of an atomic adsorbate.[11,21,23] Therefore, our works consider these triatomic ensembles for the evaluation of alloying effects. Figure 2.1 shows the triatomic ensembles of $X_xAu_{1-x}(111)$ (X = Pd, Rh, and Pt) random alloy surfaces. For each bimetallic, four different triatomic ensembles (Au_3, X_1Au_2, X_2Au_1, and X_3) were studied. Our results indicate that although tuning the strain (lattice constant) or the number of alloy-substituted sublayers (electronics) of the catalytic surface could lead to the change of adsorbate binding, the adsorbate binding is still majorly determined by the composition of a triatomic ensemble (Figures 2.2 and 2.3). These clearly indicate that ensemble effect is predominant for determining the H and O bindings at the surfaces alloyed by the elements with strong and weak adsorption properties, because it is a specific ensemble (binding site) that directly provides the adsorption environment of an adsorbate.

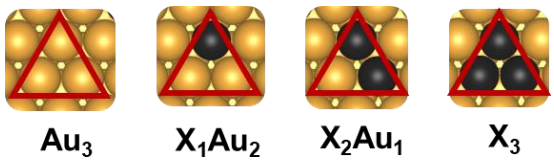

Figure 2.1: Triatomic ensembles considered as the binding sites for H and O. The black and yellow spheres represent the element X and Au, respectively. Reproduced with permission from Ref.[4].

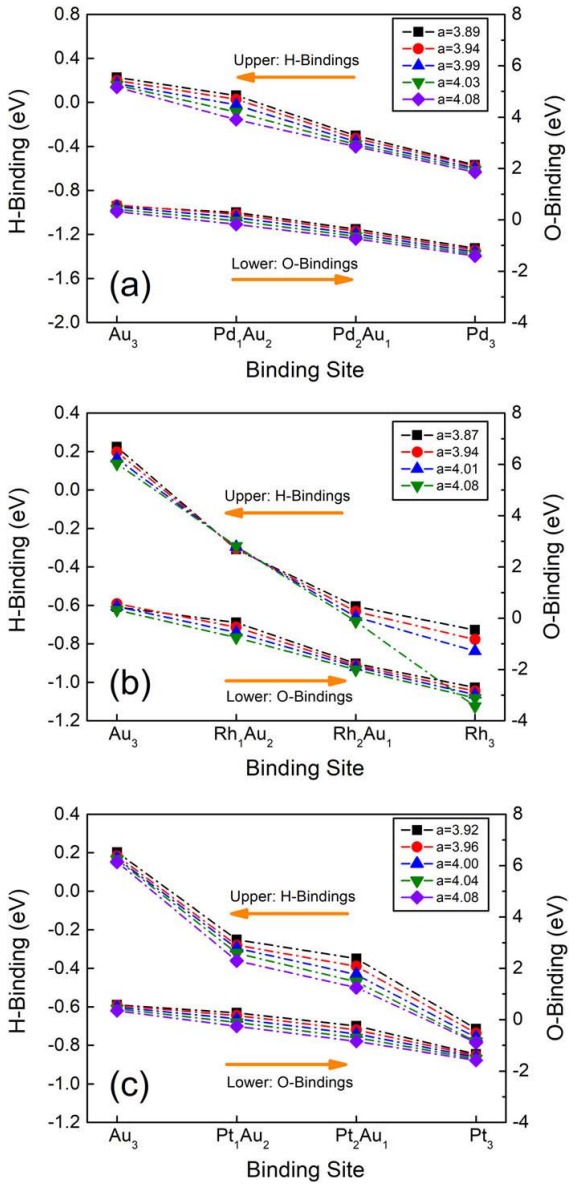

Figure 2.2: Calculated H and O binding energies at ordered alloy surfaces with varying lattice constants. (a) PdAu/Au(111), (b) RhAu/Au(111), and (c) PtAu/Au(111). The black, red, blue, green, and purple symbols represent the surfaces with varying lattice constants from that of X (X = Pd, Rh, and Pt) to Au (4.08 Å). Reproduced with permission from Ref.[4].

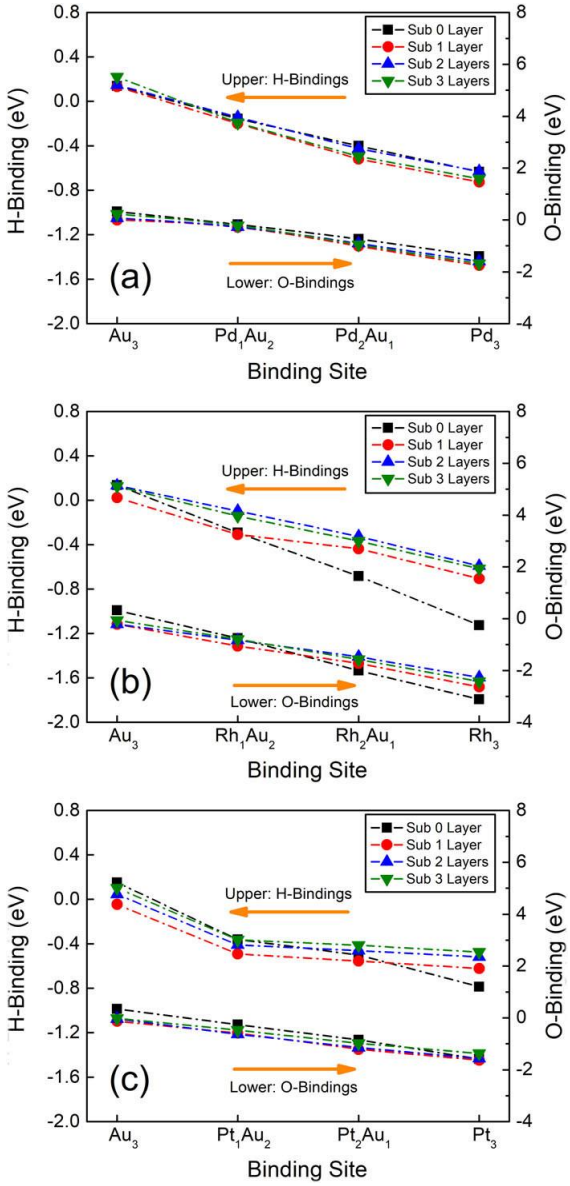

Figure 2.3: Calculated H and O binding energies at ordered alloy surfaces with varying numbers of substituted sublayers. (a) PdAu/Au(111), (b) RhAu/Au(111), and (c) PtAu/Au(111). Red, blue, and green points represent the substitution of the first 1, 2, and 3 sublayers with X(111) (X = Pd, Rh, and Pt). Reproduced with permission from Ref.[4].

Interestingly, while the H binding energies at PdAu and RhAu tend to be stronger (more negative) with the increased ratio of Pd or Rh in a triatomic ensemble, PtAu shows

less tunable H binding at those Pt-related ensembles (Figures 2.3). It can be seen from the DFT-optimized adsorption geometries that being different from those at PdAu and RhAu, H tends to migrate from the 3-fold hollow to Pt-atop or Pt_2-bridge sites at the PtAu surfaces (Figure 2.4). This suggests that alloying Pt with Au does not significantly influence H adsorption, leading to a less tunable feature of H bindings. However, in terms of the O bindings, all of the studied triatomic ensembles adsorb O at the 3-fold hollow. These interesting phenomena in theory can be qualitatively explained by the misalignment of the *d*-electrons of PtAu surface after alloying, which in turn makes the H adsorption behaves differently.

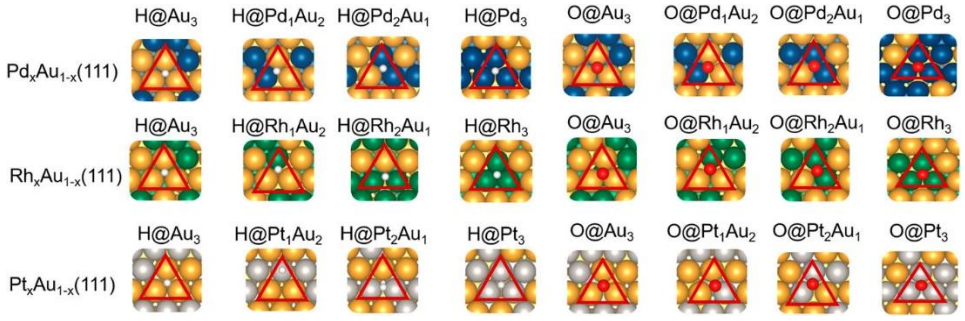

Figure 2.4: H and O binding configurations at the triatomic ensembles of $X_xAu_{1-x}(111)$ (X = Pd, Rh, and Pt) random alloy surfaces. White, red, gold, blue, green, and silver represent H, O, Au, Pd, Rh, and Pt, respectively. Reproduced with permission from Ref.[4].

With the alloying effects discussed above, we further evaluated the H and O bindings on the random alloy surfaces with the functions of ensemble compositions (Figure 2.5), with the reason that randomly alloyed geometries are similar to those alloy catalysts after a kinetically-controlled synthesis. With the relatively small error bars after sampling ten binding sites, it can be concluded that compared to the ensemble effect, the electronic and strain effects are less significant. More results and discussion can be found in Ref.[4].

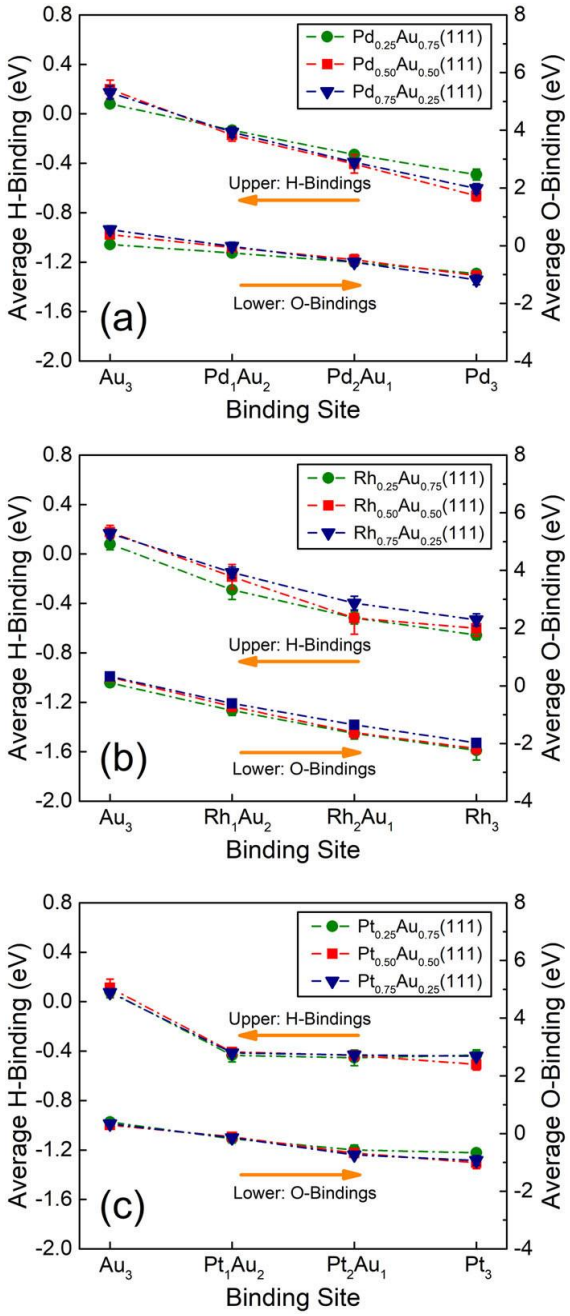

Figure 2.5: Calculated H and O binding energies on randomly alloyed (111) surfaces. H and O bindings were calculated at (a) Pd_xAu_{1-x}, (b) Rh_xAu_{1-x}, and (c) Pt_xAu_{1-x}. Each error bar was calculated from ten sampled binding sites. Reproduced with permission from Ref.[4].

2.4 THE *TUNABILITY* THEORY

Based on the results discussed above, we developed a *Tunability* theory that quantifies the tuning of adsorbate bindings on the specific atomic ensembles at alloy surfaces, which shows the predictive power of theory for experiments. A notable example of this theory is the different tunabilities of H binding between the Au surfaces alloyed with *4d* and *5d* transition metals. For the Au-alloys with *4d* "strong-binding" metals (e.g., Pd), there is a tunable trend of H binding with the increased ratio of these *4d* transition metals in a 3-fold hollow site. But differently, there is a misalignment of the *5d*-electrons after alloying and a stronger interaction of H at the surface atop site, which leads to a unique migration effect of H from the 3-fold hollow to the Pt-atop. As a result, these lead to untunable H binding at the Pt-related sites on PtAu alloy surfaces.

One of the significant applications of this theory is the hydrogenation reaction of allyl alcohol (AA) on PdAu and PtAu nanoparticles (NPs).[15] A volcano activity plot of AA hydrogenation shows that all of the plotted transition metals bind H either too strongly or too weakly to be active (Figure 2.6a). To design a catalyst with enhanced activity, our theory indicates that PdAu NPs have the alloy ensembles reaching the volcano peak, while none of the PtAu alloy ensembles can get close to this peak (Figure 2.6b). These theoretical results predict that the PdAu alloy NPs can be better catalysts as compared to pure Pd NPs, while PtAu NPs do not possess enhanced performance as compared to pure Pt NPs. These predictions have excellent agreements with our subsequent experimental studies on randomly alloyed PdAu and PtAu NPs for AA hydrogenation (Figure 2.6c). We also studied other bimetallics for C=C hydrogenation reactions using combined theoretical and experimental methods;[9,11,16,18] most of them show good agreement with the theory.

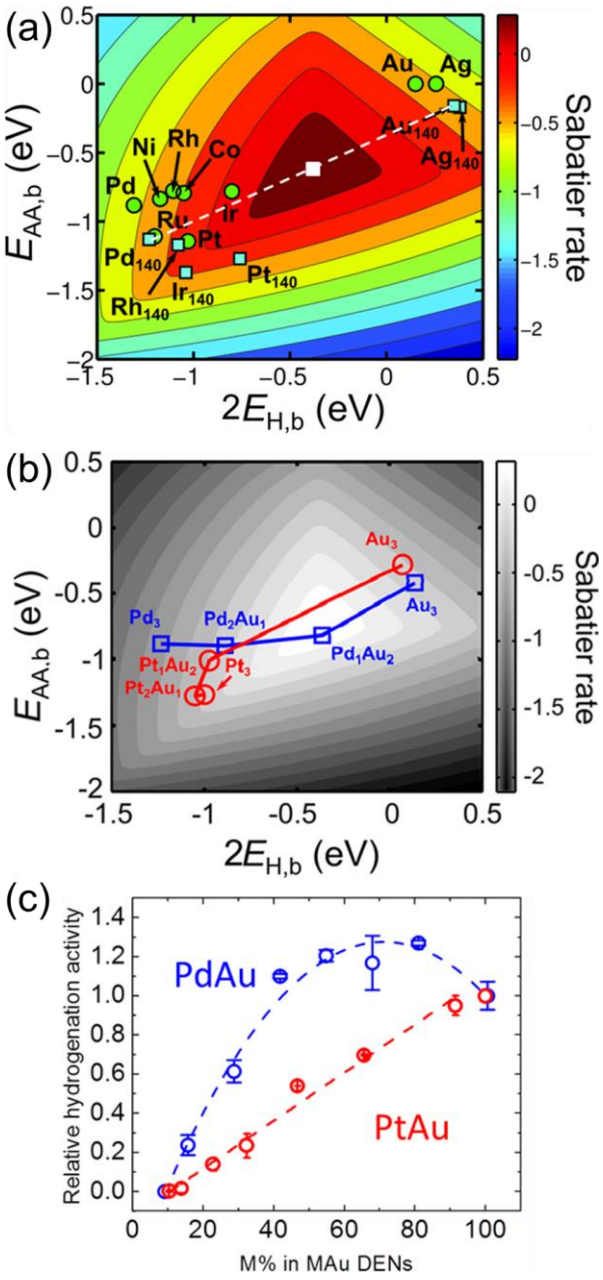

Figure 2.6: (a & b) Contour plots of the Sabatier rate as a function of H and AA binding energies on (a) bulk metals, 140-atom clusters, and (b) Pt_xAu_{1-x} and Pd_xAu_{1-x} ensembles. Each error bar was calculated from ten sampled binding sites. (c) Experimental relative AA hydrogenation turnover frequency on Pt_xAu_{1-x} and Pd_xAu_{1-x} NPs. Reproduced with permission from Ref.[15].

2.5 Conclusion

In these studies, we have shown that the atomic ensemble effect is most predominant for determining the H and O binding energies on the bimetallic surfaces alloyed by “strong-” and “weak-binding” elements. Using these knowledge from theory, we have successfully explained and predicted those bimetallic catalysts with enhanced C=C hydrogenation performances. We expect that this *Tunability* theory can be further extended to the studies on other catalytic materials and reactions.

2.6 Acknowledgement

I’m grateful to Mr. Hongyu Guo, Dr. Kihyun Shin, Prof. Long Luo, Prof. Simon Humphrey, and Prof. Richard M. Crooks for their tremendous contributions to these works. The computations were done at NERSC and TACC.

Chapter 3: Rational Design of Alloy Catalysts: Electrocatalysis*

3.1 INTRODUCTION

The study of electrocatalysis has been a hot spot in the catalyst community, with the hope of developing high-performance fuel cells and/or making full use of the inexpensive renewable energy as the electricity supply. As a key reaction in proton exchange membrane fuel cell (PEMFC) in an electrochemical device, oxygen reduction reaction (ORR) has been one of the most widely studied electrocatalytic reactions.[29] Currently, expensive Pt-catalysts are still the most commonly used ORR catalysts in industry,[30] because looking for alternatives that could potentially replace Pt is still challenging. However, in many of the previous reports, trial-and-error is still the most common strategy to search for promising ORR catalysts.

The catalytic properties of classically immiscible alloys are less studied than those miscible alloys, with one of the reasons that they have larger difficulties in synthesis and stabilization. Fortunately, with advanced kinetically-controlled synthesis methods, meta-stable alloy nanostructures of those bulk-immiscible bimetallics can be synthesized.[21] In this study, using DFT calculations and catalytic modeling methods, we predicted the ORR activities at those classically immiscible bimetallics, and found that some bulk-immiscible alloys have enhanced activities over pure metals for the ORR.[2] Picking RhAu as an example, the theoretical predictions were experimentally verified using a microwave-assisted synthesis method and the comprehensive catalytic tests.

3.2 COMPUTATIONAL METHODS

Spin-polarized DFT calculations were performed with the VASP code. KS wave functions were expanded in a plane wave basis to describe the valence electrons with the energy cutoff set as 400 eV.[25] The GGA method with PBE functional was employed to

* Li, H.; Luo, L.; Kunal, P.; Bonifacio, C. S.; Duan, Z.; Yang, J. C.; Humphrey, S. M.; Crooks, R. M.; Henkelman, G. *J. Phys. Chem. C* **2018**, 122 (5), 2712–2716; Li, H. proposed the idea, designed the research, conducted the modeling and DFT calculations, and wrote the paper.

describe electronic exchange and correlation.[26] A PAW method was employed to describe core electrons.[27] Geometries were considered optimized when all the forces in the atomistic system fell below 0.05 eV/Å. The Brillouin zone was sampled by a (3 × 3 × 1) MP *k*-point mesh.[28] Experimental and additional computational and modeling details can be found in Ref.[2].

3.3 Results and Discussion

To quickly screen the ORR activity of a catalytic surface, Nørskov et al. developed a volcano activity plot with the functions of O and OH binding energies.[31] In our study, using this volcano-like model, we found that although pure Rh and Au are almost inactive for ORR, alloying Rh with Au can lead to a Rh_1Au_2 ensemble that gets close to the volcano peak (Figure 3.1, inset). Therefore, we predicted that though RhAu is a classically immiscible bimetallic, the RhAu meta-stable alloy NPs could possess promising ORR activity (Figure 3.1).

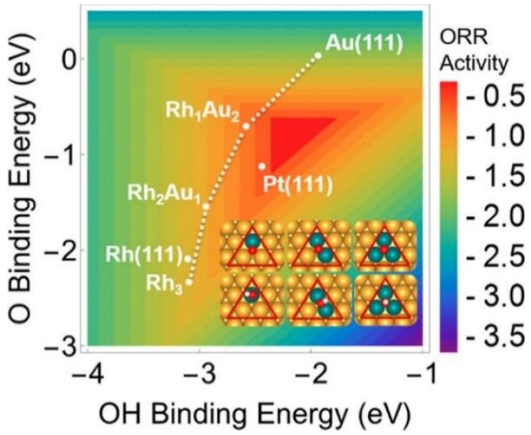

Figure 3.1: Calculated O and OH binding energies at RhAu triatomic ensembles. The inset shows the optimal binding configurations of O and OH at different triatomic ensembles. Gold, teal, red, and white spheres represent Au, Rh, O, and H, respectively. Reproduced with permission from Ref.[2].

Based on the predictions, we successfully synthesized the meta-stable RhAu alloy NPs with various compositions, using a microwave-assisted synthesis method. Our ORR

catalytic tests clearly indicated that all of the RhAu alloys showed enhanced performances, significantly outperforming the pure Au and Rh NPs (Figure 3.2). These results show good agreements with our theoretical predictions. More importantly, this case study shows that identifying the active alloy ensembles can provide predictive power to the design of new alloy catalysts. More details of the study can be found in Ref.[2].

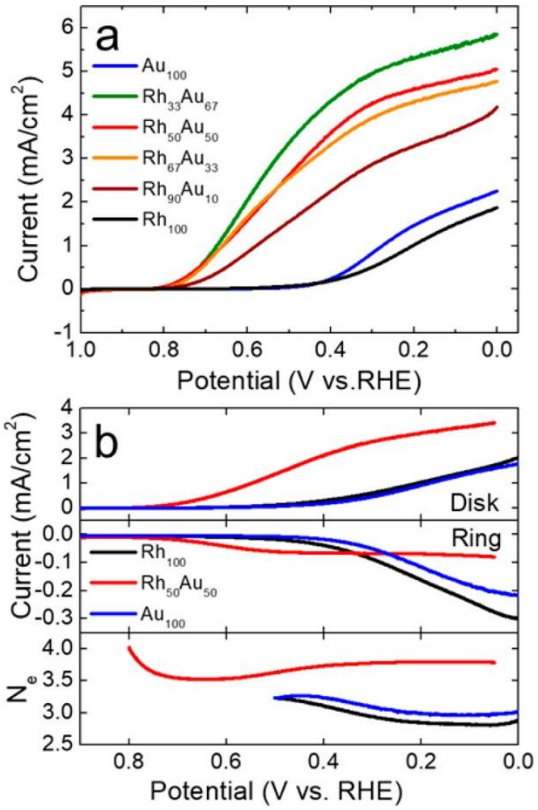

Figure 3.2: (a) ORR polarization curves for Rh_xAu_{100-x} NPs (x = 0, 33, 50, 67, 90, and 100). (b) Rotating ring-disk voltammetry of Rh_{100}, $Rh_{50}Au_{50}$, and Au_{100} modified glassy carbon electrodes. The top, middle, and bottom frames represent the disk currents arising from ORR, ring current from the oxidation of hydrogen peroxide generated at the disk electrode, and the apparent number of electrons calculated from the disk and ring currents, respectively. Reproduced with permission from Ref.[2].

3.4 Conclusion

In this study, we have shown that those less-explored classically immiscible bimetallics can be potentially used as promising ORR catalysts. Using a combined theoretical and experimental strategy, we have successfully identified the enhanced catalytic properties of RhAu meta-stable alloy NPs, as compared to pure Rh and Au NPs.

3.5 Acknowledgement

I'm grateful to Prof. Long Luo, Prof. Judith C. Yang, Prof. Simon Humphrey, and Prof. Richard M. Crooks for their tremendous contributions to these works. The computations were done at NERSC and TACC.

Chapter 4: Rational Design of Alloy Catalysts: Vapor-Phase Reactions

4.1 Introduction

Vapor-phase catalysis is an important part in the traditional industry. As one of the crucial applications of vapor-phase reaction, alcohol steam reforming has attracted much attention during the past decades with the ultimate goals of producing hydrogen or other higher-value products.[32] Ethanol (EtOH) is a type of alcohol that can be vastly produced from fermentation.[33] Though there was a large number of studies focusing on EtOH steam reforming using monometallic catalysts,[32,34] the use of alloy catalysts was less-explored. Meanwhile, gaining a theoretical understanding of the alloying effects for EtOH decomposition and oxidation is particularly challenging due to the complicated reaction steps.

In our works, using DFT calculations, catalytic modeling, and ultra-high vacuum (UHV) experiments, we studied EtOH decomposition and partial oxidation on Pd-Au model catalysts. These mechanistic insights consist of three parts: i) hydrogen production from EtOH dehydrogenation,[7] ii) EtOH decomposition,[3] and iii) EtOH partial oxidation.[5,6,8] Notably, we found that as compared to those monometallic surfaces, some alloy surfaces possess enhanced EtOH activation activities and unique reaction selectivities.

4.2 Computational Methods

The DFT calculations were performed with the VASP code. KS wave functions were expanded in a plane wave basis to describe the valence electrons.[25] The GGA method with PBE functional was employed to describe electronic exchange and correlation.[26] A PAW method was employed to describe core electrons.[27] Geometries were considered optimized when all the forces in the atomistic system fell below 0.05 eV/Å. The Brillouin zone was sampled by a (3 × 3 × 1) MP *k*-point mesh.[28] The energy barriers were calculated

using a climbing image nudged elastic band (Cl-NEB) method.[35] Experimental and additional computational and modeling details can be found in Refs.[3,5–8].

4.3 Results and Discussion

The studied model catalysts of Pd-Au were prepared in an UHV by depositing different numbers of initial monolayers (MLs) of Pd on a Au(111) single-crystal surface. After high-temperature annealing, Pd atoms were partly mixed with Au, forming a Pd-Au alloy surface. Using H_2 temperature-programmed desorption (H_2-TPD), we measured the amount of surface sites based on the intensities of two H_2 desorption peaks. The two different sites are respectively the Pd-Au interface sites (with lower H_2 desorption temperature) and the Pd(111)-like sites (with higher H_2 desorption temperature).[36] It can be clearly seen that the surface initially covered with 1-4 MLs of Pd would eventually lead to very different compositions of the two types of sites (Figure 4.1).

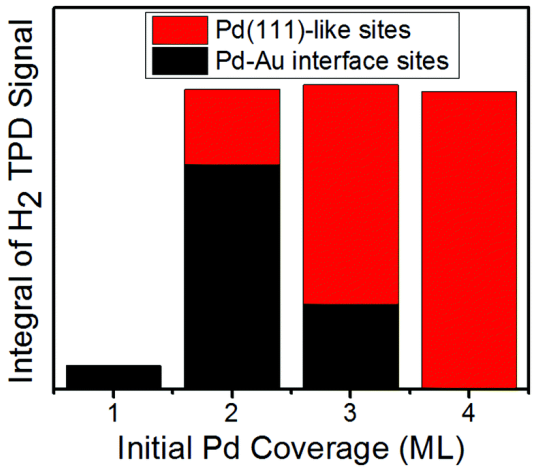

Figure 4.1: The amount of Pd-Au interface and Pd(111)-like sites on the studied Pd-Au alloy surfaces in UHV, measured from H_2-TPD experiments. Reproduced from Ref.[7] with permission from the PCCP Owner Societies.

4.3.1 Hydrogen Production from Ethanol Dehydrogenation*

Firstly, we studied the hydrogen production from EtOH dehydrogenation, on the Pd-Au model catalysts with varying Pd-Au surface compositions (Figure 4.2). Interestingly, the Pd-Au interface sites show selective hydrogen production, while a surface dominated by the Pd-Au interface together with a few Pd(111)-like sites shows the highest productions of both H_2 and CO, outperforming those surfaces dominated by the Pd(111)-like sites. These results suggest that Pd-Au alloy surfaces can either have good H_2 production selectivity or high H_2 production, outperforming pure Pd surfaces.

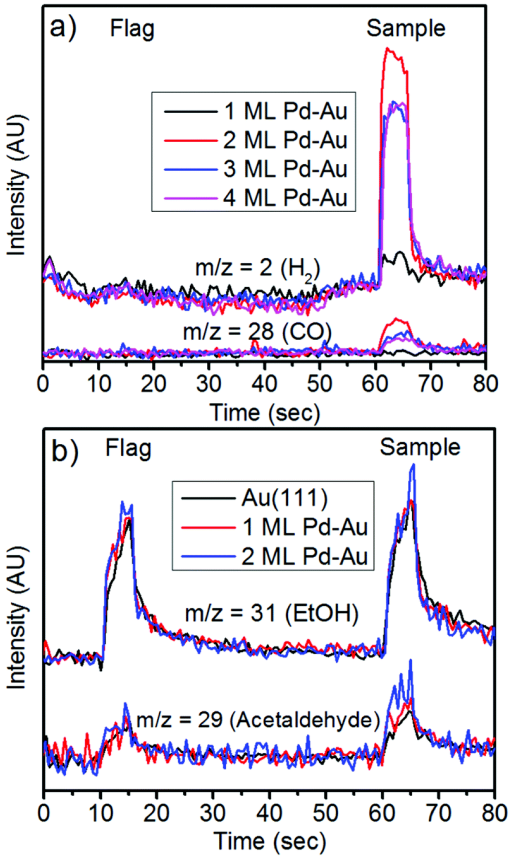

Figure 4.2: (a) H_2 and CO production and (b) ethanol desorption and acetaldehyde production from modified King and Wells experiments. Reproduced from Ref.[7] with permission from the PCCP Owner Societies.

* Evans, E. J.; Li, H.; Yu, W.-Y.; Mullen, G. M.; Henkelman, G.; Mullins, C. B. *Phys. Chem. Chem. Phys.* **2017**, 19 (45), 30578–30589; Li, H. conducted the modeling and DFT calculations and wrote the theoretical sections of the paper.

To understand these experimental results, DFT was performed to study the hydrogen associative desorption at various Pd_x/Au(111) surface ensembles (Figure 4.3). Interestingly, we can see that small Pd-Au ensembles (x=1-3) show significantly lower barriers for hydrogen desorption, indicating that those Pd-Au interface sites possess more facile hydrogen desorption kinetics, which in turns leads to larger hydrogen production detected from the experiments. Together with the fact that Au is inert for EtOH dehydrogenation, the enhanced performance in hydrogen production from EtOH dehydrogenation on Pd-Au originated in the bifunctional effects where the Pd-sites are facile for EtOH dehydrogenation, and the Pd-Au interface sites help in facile desorption of hydrogen.

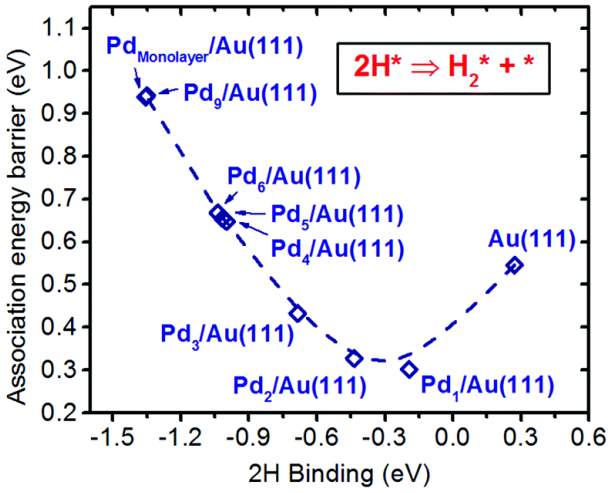

Figure 4.3: Hydrogen associative desorption energy barrier vs H binding energy on Pd-Au with varying Pd ensemble sizes. Reproduced from Ref.[7] with permission from the PCCP Owner Societies.

4.3.2 Ethanol Decomposition*

With the knowledge of hydrogen production from EtOH dehydrogenation, we further evaluated EtOH complete decomposition on Pd-Au model catalysts. From a comprehensive catalytic modeling based on the Brønsted-Evans-Polanyi (BEP) relationships[37] (details can be found in Ref.[3]), our results show that a $Pd_2Au_1(111)$ surface has higher theoretical activity than the $Pd_1Au_2(111)$ and $Pd_{ML}(111)$ surfaces (Figure 4.4). The well-tuned carbon binding energies with varying Pd compositions indicate that alloying Pd with Au can reduce carbon coking during the reactions (Figure 4.5). These modeling results suggest that $Pd_2Au_1(111)$ is an ideal surface for EtOH decomposition.

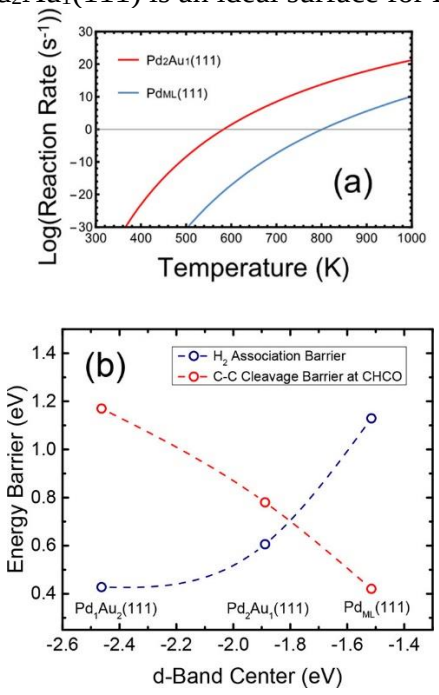

Figure 4.4: (a) Calculated reaction rates of ethanol C–C bond cleavage on $Pd_2Au_1(111)$ and $Pd_{ML}(111)$. (b) Calculated *d*-band center vs activation energies for hydrogen associative desorption and C−C bond cleavage at the CHCO species. Reproduced with permission from Ref.[3].

* Li, H.; Evans, E. J.; Mullins, C. B.; Henkelman, G. *J. Phys. Chem. C* **2018**, 122, 22024–22032; Li, H. proposed the idea, designed the research, conducted the modeling and DFT calculations, and wrote the paper along with Evans, E. J.

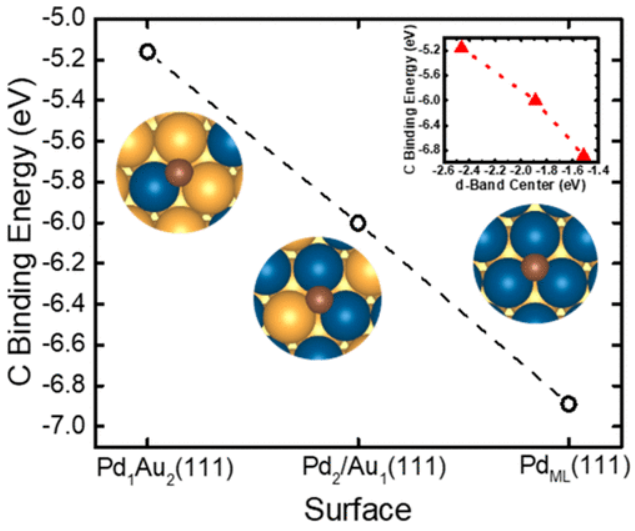

Figure 4.5: Carbon binding energy on the three different Pd-Au alloy surfaces. Inset shows the plot of carbon binding energy vs calculated *d*-band center. Blue, gold, and brown spheres represent Pd, Au, and C, respectively. Reproduced with permission from Ref.[3].

To verify our theoretical predictions, EtOH decomposition experiments were performed on Pd-Au and Au(111) model catalysts. The 2 and 4 ML Pd-Au catalysts in Figure 4.6 represent the Au (111) surfaces initially covered with 2 and 4 MLs of Pd, respectively. According to the H_2-TPD measurements in Figure 4.1, the 2 ML Pd-Au catalyst represents the hybrid of the $Pd_2Au_1(111)$ and $Pd_{ML}(111)$, while the 4 ML Pd-Au catalyst represents a $Pd_{ML}(111)$. Interestingly, our modified King and Wells experiments showed that the 2 ML Pd-Au catalyst had the highest production of methane, outperforming Au(111) and the 4 ML Pd-Au catalyst. These results have good agreements with our theoretical expectations that a catalytic surface dominated by the Pd-Au interface sites has good EtOH decomposition activity, due to the active EtOH decomposition, facile hydrogen desorption, and less carbon coking. Additional experimental details can be found in Ref.[3].

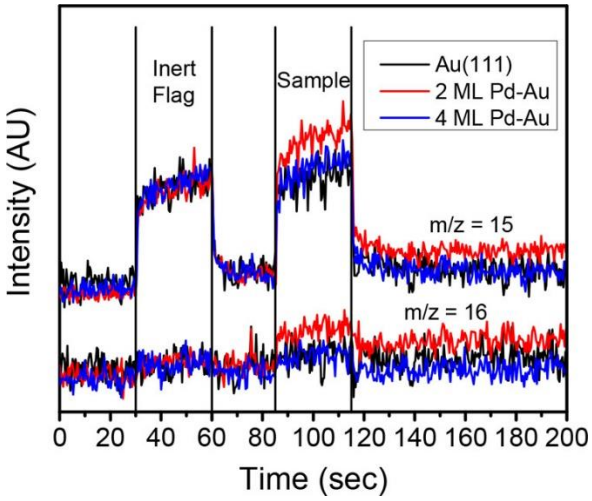

Figure 4.6: Methane spectra of a modified King and Wells experiment in which ethanol was impinged on the Au(111), 2 ML Pd–Au, and 4 ML Pd–Au. Reproduced with permission from Ref.[3].

4.3.3 Ethanol Partial Oxidation*

Compared to complete decomposition, the EtOH partial oxidation is a process that can produce higher-value products such as acetic acid and ethyl acetate.[38] Using DFT calculations, we surprisingly found that different sizes and geometries of PdAu and RhAu alloy ensembles can lead to very different activities and selectivities for EtOH partial oxidation (Figure 4.7).[6] Meanwhile, the unwanted β-C-H activation is found to be more favorable in many PdAu and RhAu ensembles. To tailor the initial dehydrogenation selectivity of EtOH, we found that a single-atom alloy catalyst with an active single-atom element (e.g., Pd, Pt, Ir, and Rh) doped onto an inert substrate (e.g., Au, Ag, and Cu (111)) can lead to a unique α-C-H activation in EtOH dehydrogenation (Figure 4.8).[5] We expect

* [1]Li, H.; Henkelman, G. A. *J. Phys. Chem. C* **2017**, 121 (49), 27504–27510; Li, H. proposed the idea, designed the research, conducted the modeling and DFT calculations, and wrote the paper. [2]Li, H.; Chai, W.; Henkelman, G. *J. Mater. Chem. A* **2019**, 7, 23868–23877; Li, H. proposed the idea, designed the research, conducted the modeling and DFT calculations, and wrote the paper. [3]Evans, E. J.; Li, H.; Henkelman, G.; Mullins, C. B. *ACS Catal.* **2019**, 9, 4516–4525; Li, H. conducted the modeling and DFT calculations and wrote the theoretical sections of the paper.

that these theoretical results can help in future catalysts design for the formation of a target product.

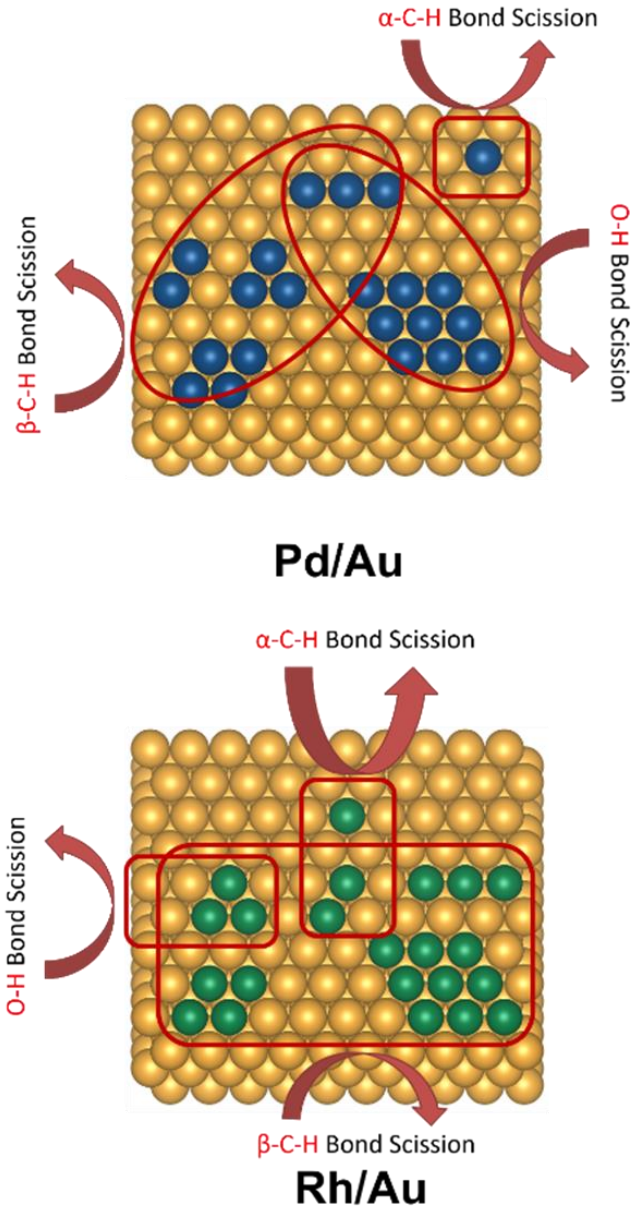

Figure 4.7: Different sizes and geometries of PdAu and RhAu surface ensembles lead to various initial dehydrogenation selectivity in ethanol partial oxidation. Reproduced with permission from Ref.[6].

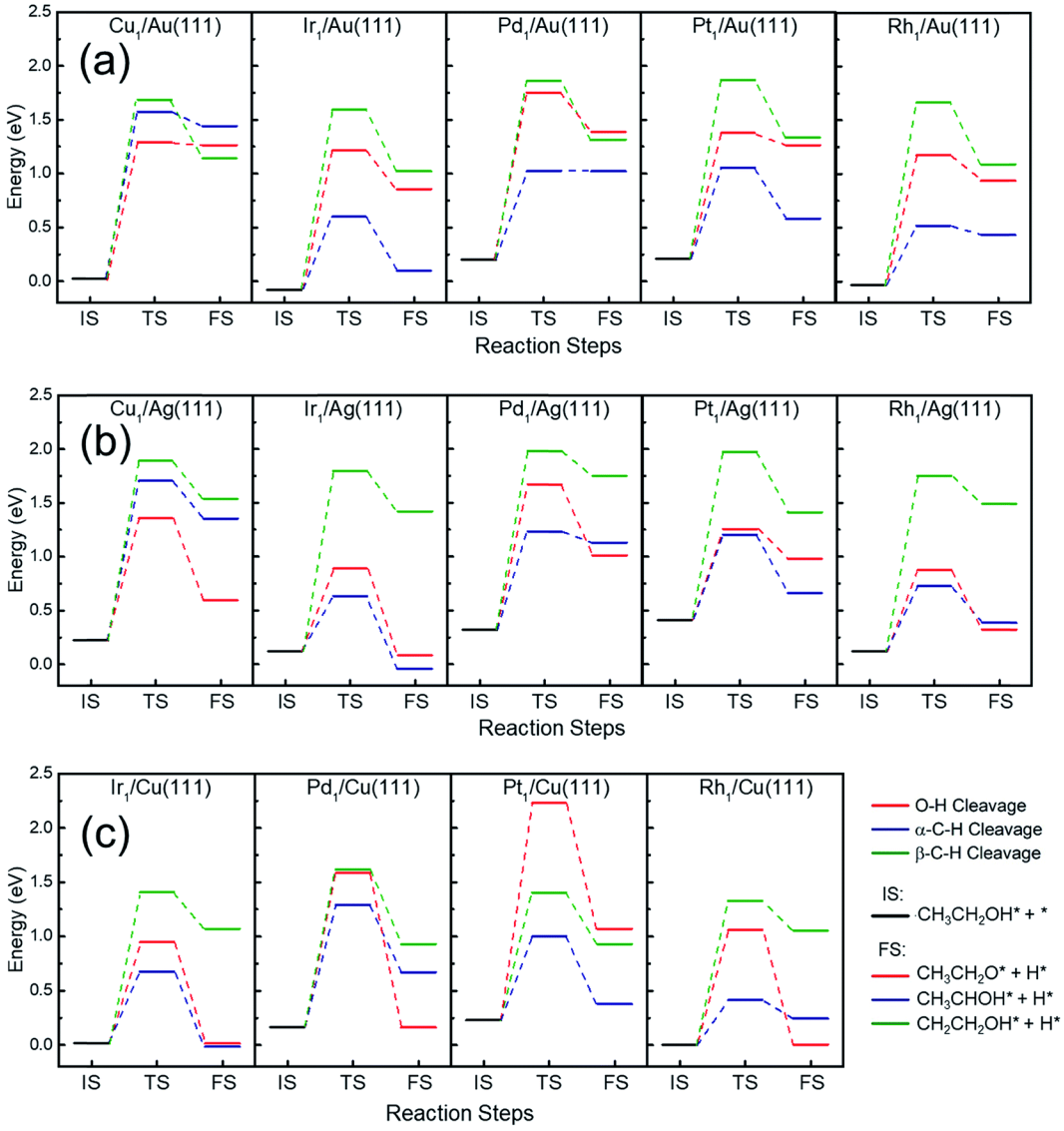

Figure 4.8: Calculated reaction pathways of ethanol initial dehydrogenation on the single-atom sites doped at (a) Au(111), (b) Ag(111), and (c) Cu(111). IS, TS, and FS represent the initial, transition, and final states, respectively. Reproduced from Ref.[5] with permission from The Royal Society of Chemistry.

Furthermore, we evaluated the EtOH partial oxidation with the presence of pre-adsorbed oxygen and hydroxyl (Figure 4.9).[8] Interestingly, we found that oxygen and hydroxyl can act as the promoter that "pulls" the hydrogen out from the α-C-H and O-H groups of the EtOH, which in turn provides higher chances for the dehydrogenated EtOH

species to react. Meanwhile, these reactions are more facile on a $Pd_2Au_1(111)$ surface, as compared to $Pd_{ML}(111)$. Evaluating the potential cross-coupling pathways of two dehydrogenated EtOH species (Figure 4.10), it is found that the formation of ethyl acetate can be facile with the pre-covered oxygen on the surface. Therefore, we expect that on a Pd-Au model catalyst, while Pd(111)-like sites are facile for oxygen activation, the presence of Pd-Au interface sites can lead to an active and selective EtOH dehydrogenation, which eventually lead to possible production of ethyl acetate.

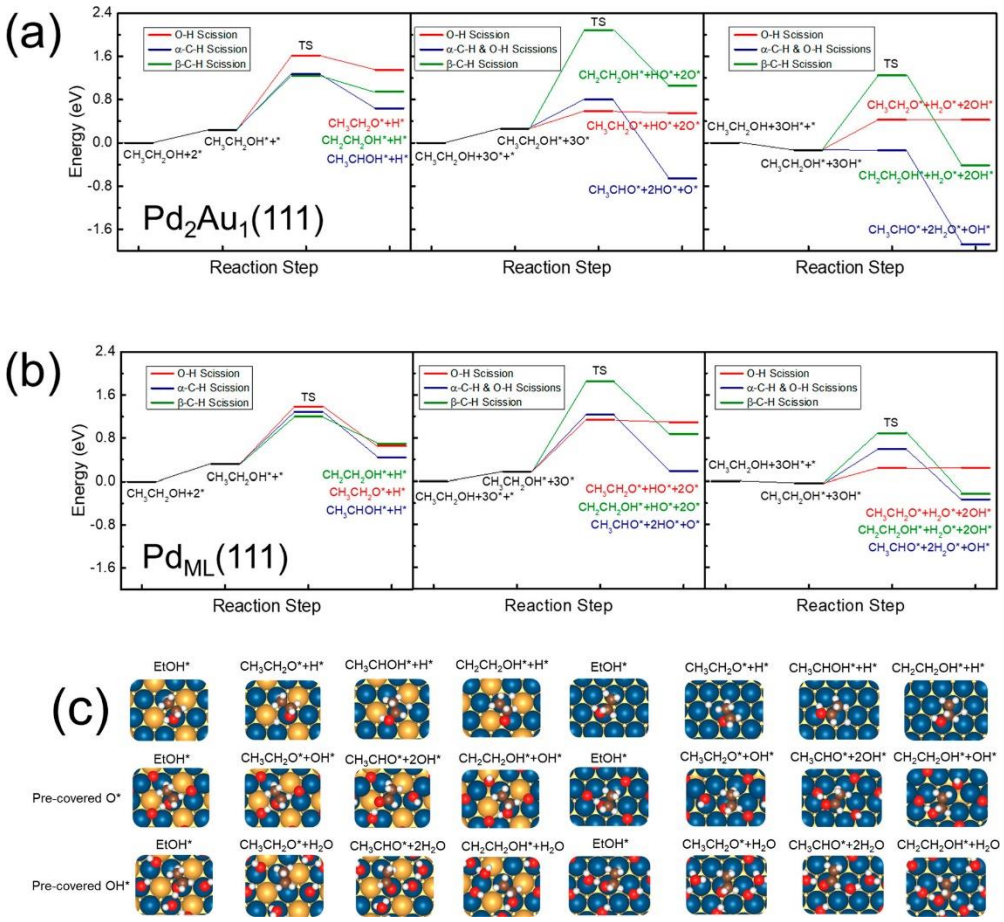

Figure 4.9: Calculated reaction pathways of ethanol initial dehydrogenation on (a) $Pd_2Au_1(111)$ and (b) $Pd_{ML}(111)$. The left, middle, and right frames represent the reactions on bare, 1/3 oxygen pre-covered, and 1/3 hydroxyl pre-covered surfaces, respectively. (c) Initial and final states of all the reactions. Blue, gold, brown, red, and white spheres represent Pd, Au, C, O, and H, respectively. Reproduced with permission from Ref.[8].

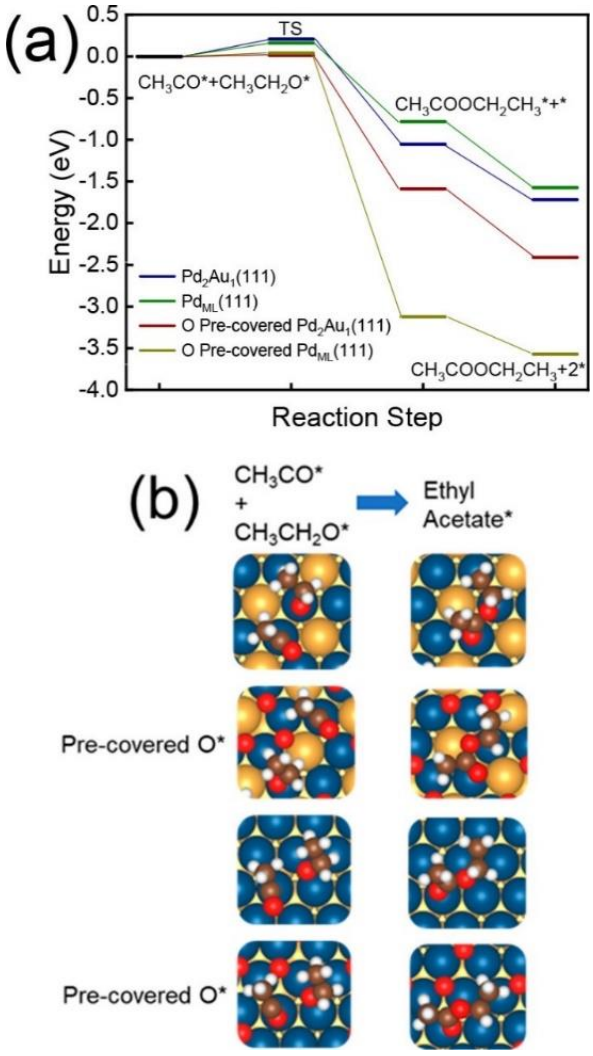

Figure 4.10: (a) Calculated reaction pathways of ethyl acetate formation through a cross-coupling mechanism on $Pd_2Au_1(111)$ and $Pd_{ML}(111)$. Both bare and 1/3 oxygen pre-covered surfaces are considered for the calculations. (b) Initial and final states of all the reactions. Blue, gold, brown, red, and white spheres represent Pd, Au, C, O, and H, respectively. Reproduced with permission from Ref.[8].

To evaluate the predictions from theory, UHV experiments were performed on Pd-Au model catalysts with the pre-activated oxygen on the surface (Figure 4.11). Excitingly, we found a facile production of ethyl acetate after the exposure of EtOH, in good agreement with our theoretical catalysts design. Additional experimental details can be found in Ref.[8].

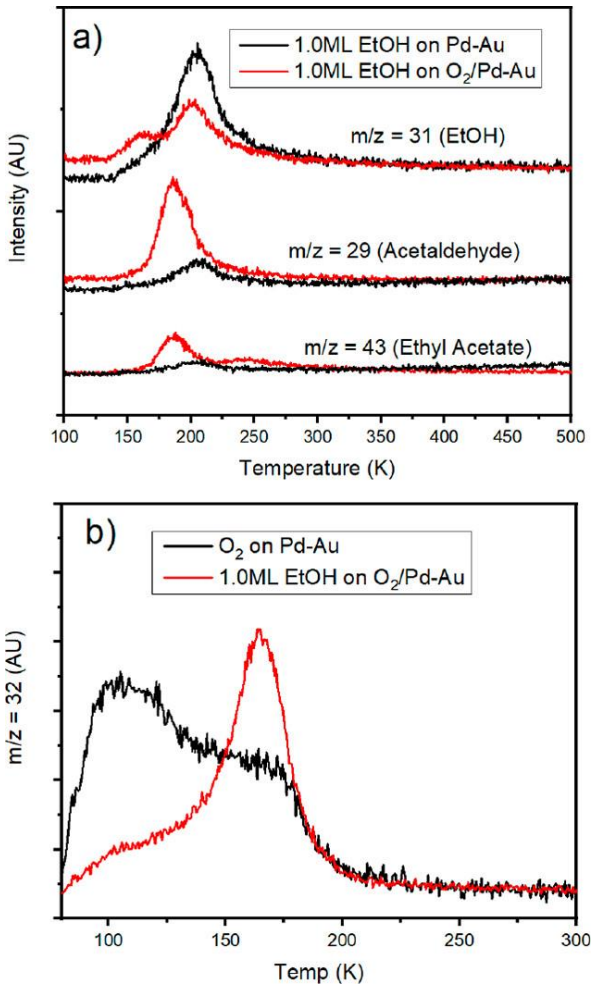

Figure 4.11: (a) Ethyl acetate and acetaldehyde production after 1.0 ML of ethanol on oxygen-covered Pd–Au. (b) Oxygen TPD with and without ethanol on Pd–Au surface. Reproduced with permission from Ref.[8].

4.4 CONCLUSION

In these studies, we have shown that some alloy surfaces possess unique activities and selectivities on EtOH dehydrogenation, decomposition, and partial oxidation, using combined theoretical and experimental techniques. In particular, we found that Pd-Au surfaces with specific compositions can lead to promising performances including selective H_2 production, facile EtOH decomposition, and the selective production of ethyl acetate.

4.5 ACKNOWLEDGEMENT

I'm grateful to Dr. Edward J. Evans and Prof. C. Buddie Mullins for their tremendous contributions to these works. The computations were done at NERSC and TACC.

Chapter 5: Rational Design of Alloy Catalysts: Liquid-Phase Reactions*

5.1 Introduction

Thermal catalytic reactions in the liquid phase are rarely explored in theoretical studies, partly because they have highly complicated reaction networks.[39] In recent years, an emerging topic of liquid-phase catalysis is water treatment. Due to the serious water contamination issues around the world, catalytic treatment in water is considered as an advanced method that could lead to less economic cost and higher efficiency.[10] As one of the most dangerous contaminants, nitrate widely distributes in groundwater, causing serious global health issues.[40] One of the most important issues is that it can be easily converted into nitrite, causing hypertension, blue baby syndrome, and even cancer.[10] However, a good catalytic design strategy for nitrite removal was not found. One of the reasons was that there is a highly complicated reaction network for catalytic nitrite reduction, resulting in either N_2 or NH_3 formation (Figure 5.1). The complexity of the reaction network leads to difficulties in understanding the reaction mechanisms on a catalytic surface.

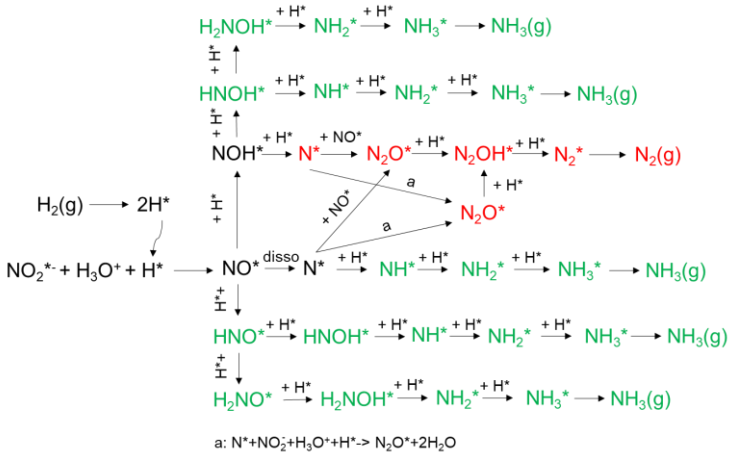

Figure 5.1: Catalytic reaction pathways for nitrite reduction. Reproduced with permission from Ref.[1].

* Li, H.; Guo, S.; Shin, K.; Henkelman, G.; Wong, M. S. *ACS Catal.* **2019**, 9 (9), 7957–7966; Li, H. proposed the idea, designed the research, conducted the modeling and DFT calculations, and wrote the paper.

To understand the trends in catalytic nitrite reduction and provide a predictive guide for experiments, here, we developed catalytic models for nitrite reduction, using N, N_2, and NH_3 binding energies as the reaction descriptors.[1] Based on the models, we identified the active sites for nitrite reduction and designed a unique structure that possesses promising catalytic activities.

5.2 COMPUTATIONAL METHODS

The DFT calculations were performed with the VASP code. KS wave functions were expanded in a plane wave basis to describe the valence electrons with the energy cutoff set as 400 eV.[25] The GGA method with PBE functional was employed to describe electronic exchange and correlation.[26] A PAW method was employed to describe core electrons.[27] Geometries were considered optimized when all the forces in the atomistic system fell below 0.05 eV/Å. The Brillouin zone was sampled by a (3 × 3 × 1) MP *k*-point mesh.[28] Spin polarization was tested and used when necessary. Experimental and additional computational and modeling details can be found in Ref.[1].

5.3 RESULTS AND DISCUSSION

Using DFT calculations and catalytic modeling, we developed two volcano activity models for nitrite reduction, respectively towards the formation selectivities of N_2 (Figure 5.2a) and NH_3 (Figure 5.2b).[1] Interestingly, both the activities of N_2 and NH_3 formations show the same trends with the tuning of N binding energy. Meanwhile, N_2 formation generally has lower reaction free energy than NH_3 formation. Notably, each volcano consists of two peaks, with the left peak representing the NO dissociative pathways and the right peak representing the NO associative pathways. Plotting the monometallic surfaces on the volcano, it can be seen that some monometallics (e.g., Ir, Ni, and Rh) bind N too strongly to be active, while those inert monometallics (Au, Ag, and Cu) bind N too weakly to be active.

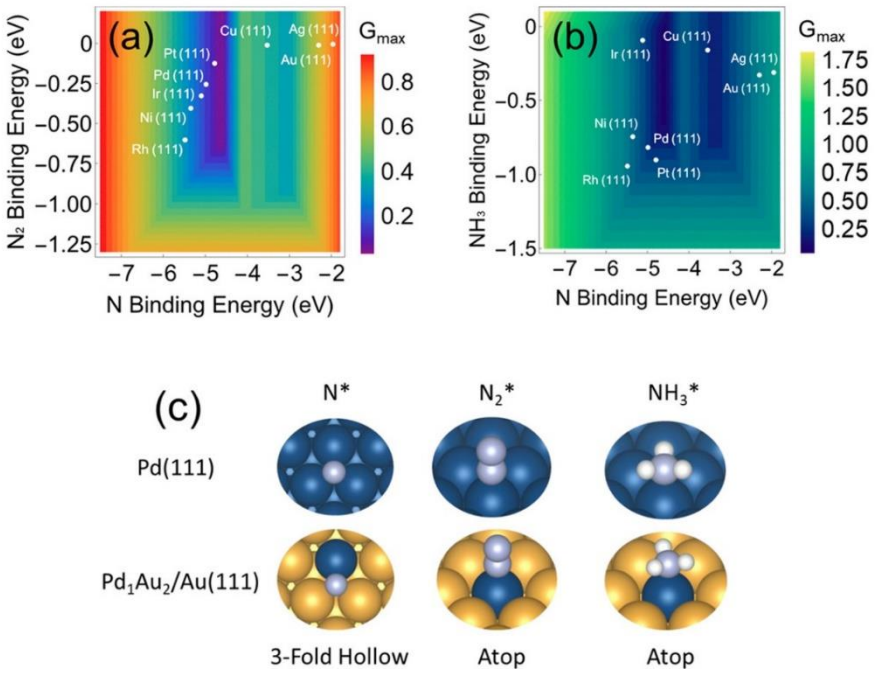

Figure 5.2: Volcano activity plots for nitrite reduction through (a) N_2 and (b) NH_3 formation pathways, with the plotted close-packed monometallic surfaces. (c) Optimized adsorption geometries of N, N_2, and NH_3 on Pd(111) and a Pd_1Au_2 3-fold triatomic ensemble. Blue, gold, white, and purple spheres represent Pd, Au, H, and N, respectively. Reproduced with permission from Ref.[1].

To verify the accuracy of the volcano model, previous experimental studies on PdAu and PdCu alloy catalysts were used to compare with our theories (Figure 5.3).[10,41] Since the N_2 selectivity is found to be more favorable than the NH_3 selectivity, and the nitrite reduction experiments on the PdAu and PdCu alloy catalysts also show the majority of N_2 formation, we only evaluate the volcano model towards N_2 formation here. Plotting the calculated N and N_2 binding energies of $Pd_xAu_{1-x}(111)$ and $Pd_xCu_{1-x}(111)$ surfaces on the volcano model, we can see that the Pd_3 triatomic ensembles are the most active sites for nitrite reduction. Besides, alloying Au or Cu with Pd can help to further optimize the reactivity of the Pd_3 ensembles. Interestingly, both the theory and experiment show that the optimal Pd% for PdAu and PdCu are ~50% and ~75%, respectively. These quantitative

agreements validate that our volcano model is relatively precise in predicting nitrite reduction activity at a catalytic surface.

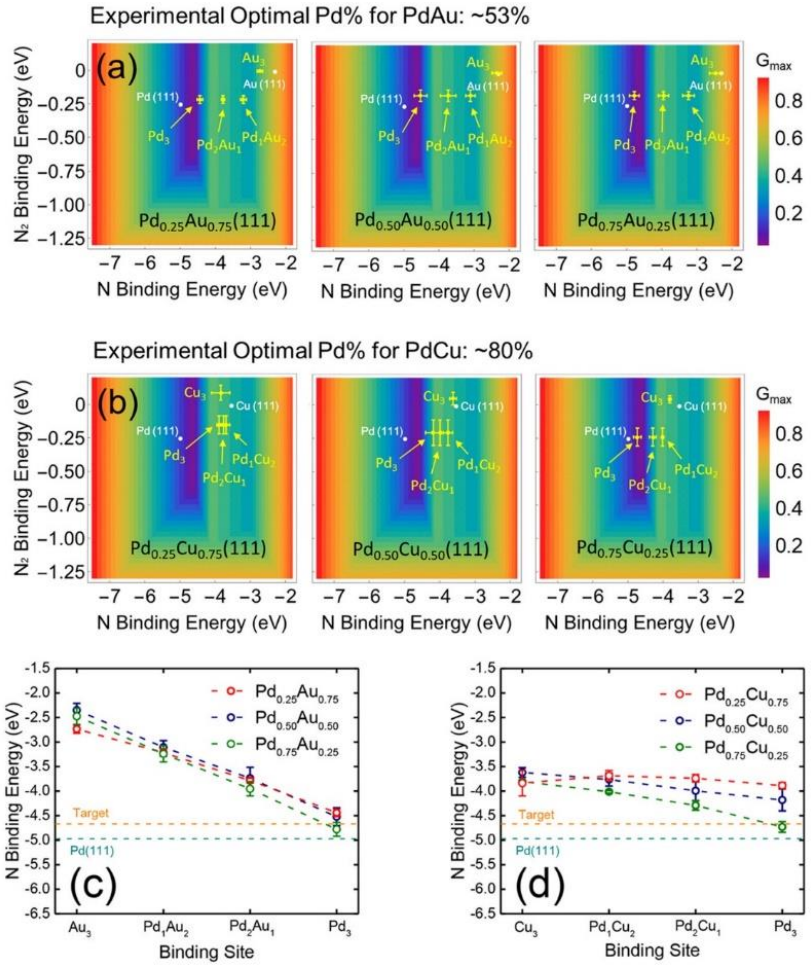

Figure 5.3: Predictions of nitrite reduction at triatomic ensembles on (a) PdAu and (b) PdCu random alloy surfaces. (c, d) Calculated average N binding energies at the triatomic ensembles of PdAu and PdCu. Each error bar was calculated from 10 sampled binding sites. Reproduced with permission from Ref.[1].

With the knowledge that pure Pd ensembles are the highly active sites, we proposed an "X-on-Y" (or core@shell) structure that can optimize the reactivity of the active sites and meanwhile, maximize the amount of these sites. Screening many X-on-Y candidates with the volcano model, we identified some core@shell structures that have the surface

sites reaching the volcano peak (Figure 5.4a and 5.4b). The calculated segregation energies indicated that most of these active structures are stable under reaction conditions (Figure 5.4c). Picking Pd-on-Au as an example, we experimentally reduced different ratios of Pd on pure Au NPs, and found that a ML of Pd covered on Au NPs can lead to an outstanding nitrite reduction activities, outperforming other Pd-Au surface compositions and pure Pd NPs (Figure 5.4d). All these experimental results are in excellent agreement with our theoretical catalysts design.

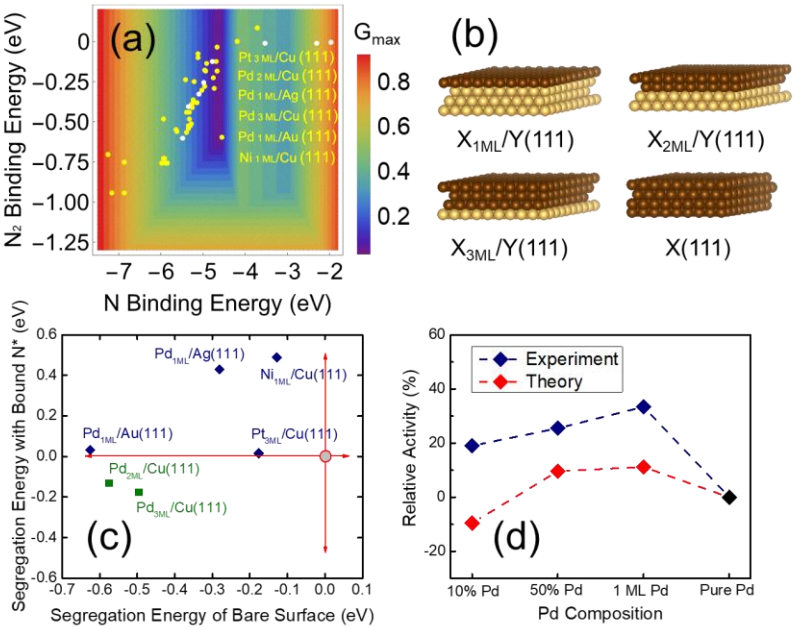

Figure 5.4: (a) Volcano activity plots of X-on-Y (X = Pd, Pt, Rh, Ir, and Ni; Y = Au, Ag, and Cu) catalysts for nitrite reduction. (b) Schematic pictures of X-on-Y catalytic models considered for calculations. Brown and gold spheres represent the X and Y elements, respectively. (c) Segregation energies with and without adsorbed N^* on the selected X-on-Y catalysts. (d) Trends of the theoretical and experimental activities for nitrite reduction. Reproduced with permission from Ref.[1].

5.4 Conclusion

In this study, for the first time, we developed an experimentally-verified catalytic model for nitrite reduction in water with the functions of N, N_2, and NH_3 binding energies. We have identified that the pure Pd ensembles are the most active sites in Pd-alloys. Based on this, we designed a core@shell structure that can optimize the reactivity of the pure Pd sites and meanwhile, maximize the number of these active sites on a catalytic surface. Our subsequent experiments verified that reducing a ML of Pd on pure Au NPs can lead to a promising nitrite reduction activity, outperforming other Pd-Au surface compositions and pure Pd NPs. Most importantly, this study shows that DFT calculations and catalytic modeling can help to address a highly complicated environmental issue such as nitrate and nitrite contamination in water.

5.5 Acknowledgement

I'm grateful to Dr. Sujin Guo, Mr. Chenxu Yan, Prof. Charles J. Werth, and Prof. Michael S. Wong for their tremendous contributions to these works. The computations were done at NERSC and TACC.

Chapter 6: Machine Learning Framework Development for Accelerating Atomistic Simulations

6.1 Introduction

DFT has demonstrated remarkable power in both the simulation of chemical processes and the prediction of materials properties owing to their high accuracy and applicability across the periodic table. Unfortunately, the computational cost of typical DFT calculations significantly increases with the increase of the size of an atomistic system. In comparison, classical force fields that fit to a specific chemical environment are able to increase simulation sizes to thousands of atoms. However, classical force fields suffer from a lack of transferability, as they have to be re-parameterized for each specific system. Therefore, our approach here is to create machine learning tools that accelerate the expensive DFT calculations that we rely on for accurately modeling materials and catalysis. Our goal is not to replace electronic structure calculations, but rather augment them with information that can be learned efficiently with modern machine learning tools. Additionally, our aim is to provide physical principles to the machine learning models, rather than rely on them entirely as a "black box". Imposing physically reasonable limits, e.g., atomic interactions, will help make machine learning models more robust outside of the immediate space where they fit and reduce the data requirements for learning the models.

As a part of the long program by the NSF Institute for Pure & Applied Mathematics (IPAM, Los Angeles) in 2017, we started developing an initial version of the machine learning framework following the Behler-Parrinello artificial neural network principle.[42] Our goal is to build an on-the-fly fitting framework of the potential energy surface (PES) to accelerate quantum-based atomistic simulations.

6.4 Results and Discussion

This machine learning framework consists of a number of independent modules, including: i) data collection (generating new structures and calculating their energies and

forces), ii) data preprocessing (filtering out the similar structures), iii) data transformation (transforming the coordinates into the fingerprints)[42], iv) data processing (correlation analysis of the inputs), and v) machine learning (model training, testing, and validation). Once the machine learning model converges, our framework can evaluate the uncertainties of the model. Those precise models will be used as the machine learning calculators, which calculate the energies and forces of those out-of-sample structures. Some of the functions in this framework are still under development. We expect that a completed version will be successfully used for global optimization of a materials structure or the screening of optimal catalytic materials for reactions in a complicated reaction network.

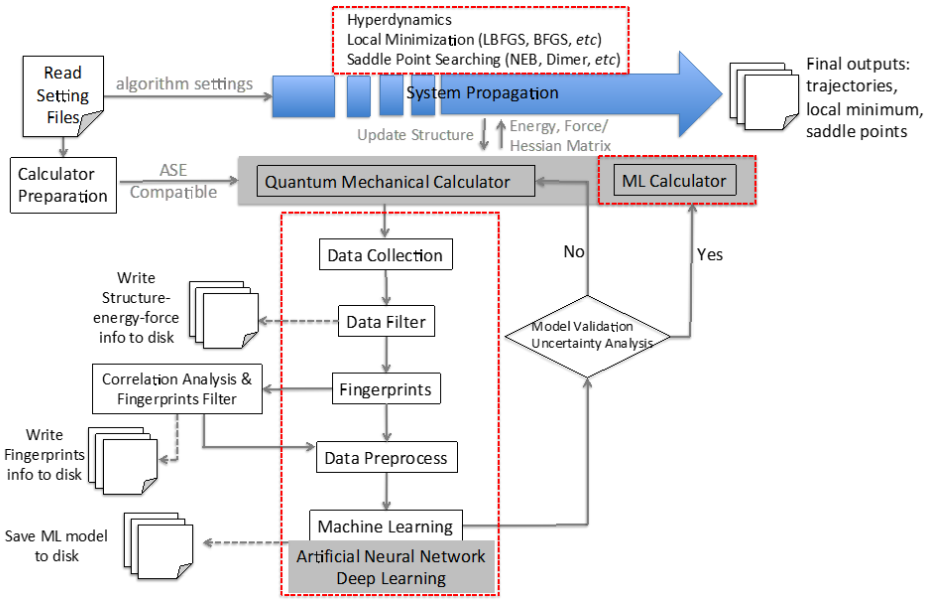

Figure 6.1: Flow chart of the machine learning framework for atomistic simulations, with the independent modules including data collection, data filter, data processing, and machine learning. Finally, the model will be saved as the machine learning calculator, to predict the energies and forces of new structures.

6.5 Conclusion

To accelerate atomistic simulation and partly replace the expensive quantum mechanical calculations, we have been developing a machine learning assisted framework that can learn from the quantum mechanical database and fit the PES of an atomistic system. We expect that this framework can help to dramatically speed-up the mechanistic understanding of chemical reactions and design high-performance materials.

6.6 Acknowledgement

I'm grateful to Mr. Stephen Xie, Dr. Anne Marie Tan, Prof. Dallas Trinkle, and Prof. Richard G. Hennig for their tremendous contributions to these works. The computations were done at NERSC and TACC.

References

(1) Li, H.; Guo, S.; Shin, K.; Henkelman, G.; Wong, M. S. *ACS Catal.* **2019**, *9* (9), 7957–7966.

(2) Li, H.; Luo, L.; Kunal, P.; Bonifacio, C. S.; Duan, Z.; Yang, J. C.; Humphrey, S. M.; Crooks, R. M.; Henkelman, G. *J. Phys. Chem. C* **2018**, *122* (5), 2712–2716.

(3) Li, H.; Evans, E. J.; Mullins, C. B.; Henkelman, G. *J. Phys. Chem. C* **2018**, *122*, 22024–22032.

(4) Li, H.; Shin, K.; Henkelman, G. *J. Chem. Phys.* **2018**, *149* (17), 174705.

(5) Li, H.; Chai, W.; Henkelman, G. *J. Mater. Chem. A* **2019**, *7*, 23868–23877.

(6) Li, H.; Henkelman, G. A. *J. Phys. Chem. C* **2017**, *121* (49), 27504–27510.

(7) Evans, E. J.; Li, H.; Yu, W.-Y.; Mullen, G. M.; Henkelman, G.; Mullins, C. B. *Phys. Chem. Chem. Phys.* **2017**, *19* (45), 30578–30589.

(8) Evans, E. J.; Li, H.; Henkelman, G.; Mullins, C. B. *ACS Catal.* **2019**, *9*, 4516–4525.

(9) Guo, H.; Li, H.; Jarvis, K.; Wan, H.; Kunal, P.; Dunning, S. G.; Liu, Y.; Henkelman, G.; Humphrey, S. M. *ACS Catal.* **2018**, *8*, 11386–11397.

(10) Seraj, S.; Kunal, P.; Li, H.; Henkelman, G.; Humphrey, S. M.; Werth, C. J. *ACS Catal.* **2017**, *7* (5), 3268–3276.

(11) Kunal, P.; Li, H.; Dewing, B. L.; Zhang, L.; Jarvis, K.; Henkelman, G.; Humphrey, S. M. *ACS Catal.* **2016**, *6* (8), 4882–4893.

(12) Guo, H.; Fang, Z.; Li, H.; Fernandez, D.; Henkelman, G.; Humphrey, S. M.; Yu, G. *ACS Nano* **2019**, *13* (11), 13225–13234.

(13) Yu, B.; Li, H.; White, J.; Donne, S.; Yi, J.; Xi, S.; Fu, Y.; Henkelman, G.; Yu, H.; Chen, Z.; Ma, T. *Adv. Funct. Mater.* **2019**, *1905665*, 1–11.

(14) Zhou, Z.; Yuan, Z.; Li, S.; Li, H.; Chen, J.; Wang, Y.; Huang, Q.; Wang, C.; Karahan, H. E.; Henkelman, G.; Liao, X.; Wei, L.; Chen, Y. *Small* **2019**, *1900358*, 1–11.

(15) Luo, L.; Duan, Z.; Li, H.; Kim, J.; Henkelman, G.; Crooks, R. M. *J. Am. Chem. Soc.* **2017**, *139*, 5538–5546.

(16) Piburn, G. W.; Li, H.; Kunal, P.; Henkelman, G.; Humphrey, S. M. *ChemCatChem* **2018**, *10* (1), 329–333.

(17) Liu, Y.; Li, H.; Cen, W.; Li, J.; Wang, Z.; Henkelman, G. *Phys. Chem. Chem. Phys.* **2018**, *20* (11), 7508–7513.

(18) Guo, H.; Li, H.; Fernandez, D.; Willis, S.; Jarvis, K.; Henkelman, G.; Humphrey, S. M. *Chem. Mater.* **2019**.

(19) House, S. D.; Bonifacio, C. S.; Timoshenko, J.; Kunal, P.; Wan, H.; Duan, Z.; Li, H.; Yang, J. C.; Frenkel, A. I.; Humphrey, S. M.; Crooks, R. M.; Henkelman, G. A. *Microsc. Microanal.* **2017**, *23* (S1), 2030–2031.

(20) Anderson, R. M.; Yancey, D. F.; Zhang, L.; Chill, S. T.; Henkelman, G.; Crooks, R. M. *Acc. Chem. Res.* **2015**, *48* (5), 1351–1357.

(21) García, S.; Zhang, L.; Piburn, G. W.; Henkelman, G.; Humphrey, S. M. *ACS Nano* **2014**, *8* (11), 11512–11521.

(22) Zhong, W.; Qi, Y.; Deng, M. *J. Power Sources* **2015**, *278*, 203–212.

(23) Liu, P.; Nørskov, J. K. *Phys. Chem. Chem. Phys.* **2001**, *3* (17), 3814–3818.
(24) Mavrikakis, M.; Hammer, B.; Nørskov, J. *Phys. Rev. Lett.* **1998**, *81* (13), 2819–2822.
(25) Kohn, W.; Sham, L. J. *Phys. Rev.* **1965**, *140* (4A), A1133.
(26) Perdew, J. P.; Burke, K.; Ernzerhof, M. *Phys. Rev. Lett.* **1996**, *77* (18), 3865–3868.
(27) Blöchl, P. E. *Phys. Rev. B* **1994**, *50* (24), 17953–17979.
(28) Monkhorst, H.; Pack, J. *Phys. Rev. B* **1976**, *13* (12), 5188–5192.
(29) Kulkarni, A.; Siahrostami, S.; Patel, A.; Nørskov, J. K. *Chem. Rev*. **2018**, *118* (5), 2302–2312.
(30) Adzic, R. R.; Zhang, J.; Sasaki, K.; Vukmirovic, M. B.; Shao, M.; Wang, J. X.; Nilekar, A. U.; Mavrikakis, M.; Valerio, J. A.; Uribe, F. *Top. Catal.* **2007**, *46* (3–4), 249–262.
(31) Nørskov, J. K.; Rossmeisl, J.; Logadottir, A.; Lindqvist, L.; Kitchin, J. R.; Bligaard, T.; Jónsson, H. *J. Phys. Chem. B* **2004**, *108* (46), 17886–17892.
(32) Zanchet, D.; Santos, J. B. O.; Damyanova, S.; Gallo, J. M. R.; Bueno, J. M. C. *ACS Catal*. **2015**, *5* (6), 3841–3863.
(33) Lin, Y.; Tanaka, S. *Appl. Microbiol. Biotechnol*. **2006**, *69* (6) 627–642.
(34) Ferrin, P.; Simonetti, D.; Kandoi, S.; Kunkes, E.; Dumesic, J. A.; Nørskov, J. K.; Mavrikakis, M. *J. Am. Chem. Soc.* **2009**, *131* (16), 5809–5815.
(35) Henkelman, G.; Uberuaga, B. P.; Jónsson, H. *J. Chem. Phys.* **2000**, *113* (22), 9901–9904.
(36) Yu, W. Y.; Mullen, G. M.; Flaherty, D. W.; Mullins, C. B. *J. Am. Chem. Soc.* **2014**, *136* (31), 11070–11078.
(37) Bligaard, T.; Nørskov, J. K.; Dahl, S.; Matthiesen, J.; Christensen, C. H.; Sehested, J. *J. Catal.* **2004**, *224* (1), 206–217.
(38) Liu, X.; Xu, B.; Haubrich, J.; Madix, R. J.; Friend, C. M. *J. Am. Chem. Soc.* **2009**, *131* (16), 5757–5759.
(39) Shin, H.; Jung, S.; Bae, S.; Lee, W.; Kim, H. *Environ. Sci. Technol.* **2014**, *48* (21), 12768–12774.
(40) Liu, A.; Ming, J.; Ankumah, R. O. *Sci. Total Environ.* **2005**, *346* (1–3), 112–120.
(41) Guy, K. A.; Xu, H.; Yang, J. C.; Werth, C. J.; Shapley, J. R. *J. Phys. Chem. C* **2009**, *113* (19), 8177–8185.
(42) Behler, J.; Parrinello, M. *Phys. Rev. Lett.* **2007**, *98* (14), 146401.